ACS OMEGA

Open Access

http://pubs.acs.org/journal/acsodf

Article

pH-Responsive Biocompatible Fluorescent Hydrogel for Selective Sensing and Adsorptive Recovery of Dysprosium

Mrinmoy Karmakar, Somya Sadaf, and Chinmay Ghoroi*

Cite This: *ACS Omega* 2024, 9, 29620−29632

Read Online

ACCESS | Metrics & More | Article Recommendations | Supporting Information

ABSTRACT: The elevated accumulation of electronic wastes, especially containing Dysprosium ion [i.e., Dy(III)], is emerging as a potential environmental threat. To overcome the deleterious effects of Dy(III), detection and removal of Dy(III) is crucial. Moreover, recovery of high-value Dy(III) is economically beneficial. However, the availability of a single material, capable of sensing Dy(III) in nanomolar concentration and simultaneously adsorbing it with high adsorption capacity (AC), is rare. Therefore, to solve this problem, a pH-responsive fluorescent amino graphene oxide-impregnated-engineered polymer hydrogel (**AGO-EPH**) has been synthesized, suitable for selective sensing of Dy(III) in nanomolar concentration and adsorbing it from wastewater at ambient temperature. This terpolymeric hydrogel is synthesized from two nonfluorescent monomers, propenoic acid (PNA) and prop-2-enamide (PEAM), along with an in situ generated comonomer (3-acrylamidopropanoic acid/AAPPA) through N−*H* activation during polymerization. Surface properties and structural details of **AGO-EPH** are established using NMR, FTIR, XRD, TEM, SEM, EDX, Raman, MALDI-mass, and DLS studies. The **AGO-EPH** exhibits blue fluorescence with *selective* turn-off sensing of Dy(III) with the detection limit of 1.88×10^{-7} (M). The maximum AC of **AGO-EPH** is 41.97 ± 0.39 mg g^{-1}. The developed **AGO-EPH** shows consistent adsorption−desorption property over five cycles, with more than 90% desorption efficiency per cycle, confirming significant recovery of the valuable Dy(III). From Logic gate calculations, complexation of Dy(III) and **AGO-EPH** may be the reason behind fluorescence quenching. The **AGO-EPH** also shows antibacterial action against $\sim 3 \times 10^8$ cells mL^{-1} of *E. coli* solution. Overall, the developed pH-responsive engineered hydrogel can be used as a potential low-cost sensing device and reusable adsorbent for Dy(III).

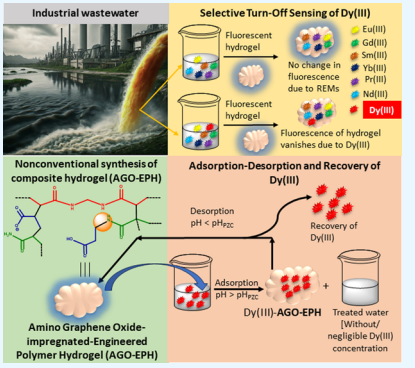

1. INTRODUCTION

Rare earth metal (REM) ions are emerging as one of the most precious materials because of their extensive use in manufacturing magnets, memory devices, and batteries.[1,2] Among different REMs, dysprosium (Dy) finds widespread modern applications as alloys for neodymium-based magnets,[3] phosphor,[4] halide discharge lamps,[5] wind turbines,[6] rechargeable NiMH batteries,[7] and catalysts.[8] Moreover, Dy(III)-nickel composite is frequently used in the control rods of nuclear reactors since it can rapidly absorb accelerated neutrons and does not swell/shrink when bombarded with neutrons for long periods.[9] Therefore, Dy(III) is considered as one of the most critical raw materials for electronics and nuclear applications by the European Commission in 2010.[10] However, the global reserve of Dy is extremely limited, and most of the mining occurs in China.[3] Therefore, the variable export of Dy by China creates imbalance in the pricing of Dy. For instance, the present cost of Dy is about 548 USD/kg against 35 USD/kg in 2003.[6] Importantly, the global Dy market is projected to reach approximately 756 million USD by 2025 with a CAGR of 5.8%.[11] Eventually, India is one of the largest importers of Dy (around 6.99 million USD/year) due to the lack of extractable quantities of this precious metal in India. Therefore, it has become essential to reduce the import amount of Dy by reutilizing the unused and/or wasted Dy of industries. Recovery of unused Dy from industrial wastewater can solve this problem. However, before recovery, identification of traces of Dy in industrial wastewater is the also critical. Nevertheless, no such technology is available currently enabling the simultaneous sensing and adsorbing of traces of Dy(III)-ions from industrial wastewater. Therefore, technology development for Dy(III) sensing, recovery, and recycling from industrial wastewater has become critical. It can save a significant import liability in the coming years.

Technological advancements have led to a surge in electronic waste, resulting in the significant release of Dy(III) into soil and groundwater. Though the maximum permissible limit for Dy(III) in drinking water is yet to be declared by any of the international health organizations, yet Dy(III) is toxic to animals and plants.[12,13] Soluble Dy(III)-salts, such as $DyCl_3$

Received: March 22, 2024
Revised: June 7, 2024
Accepted: June 12, 2024
Published: June 27, 2024

and $Dy(NO_3)_3$, exhibited mild toxicity to human and aquatic plant cells, whereas the insoluble salts are nontoxic.[13] Depending on the toxicity profile of Dy(III) to mice, it is estimated that the ingestion of 500 mg or more will be fatal to human being.[13] Moreover, Dy(III)-powder explodes frequently in the presence of an ignition source when admixed to the atmosphere.[14] Importantly, fires caused from Dy-vapor cannot be extinguished by water, since it reacts with water to generate flammable hydrogen gas.[14] Therefore, isolation of Dy(III) not only saves the environment from pollution, but also enables the reuse of very rare and costly Dy(III). Therefore, detecting and removing Dy(III) from electronic wastes have become crucial.

In literature, detection of Dy(III) has been attempted using atomic absorption spectrometry,[15] inductively coupled plasma atomic emission spectroscopy,[16,17] ion selective electrode sensing,[18,19] chromatography,[20,21] resonance light scattering,[22] optical sensing,[23] and electrochemistry.[24,25] However, these methods are expensive, time-consuming, nonselective toward Dy(III), and require sophisticated instrumentation for detection. Moreover, the detection limits by these methodologies are quite high, i.e., of the order of 0.4 ppm. However, fluorescence-based turn-off sensing of cations is very rapid, selective, and sensitive.[26] In this context, Jianjun et al.[27] applied fluorescence-based detection of Dy(III) by using inorganic complexes, in which the detecting material could not be isolated after reacting with Dy(III)-solution (destructive sensing). To the best of our knowledge, there is still no report discussing reusable, efficient, rapid, and selective polymer-based sensing hydrogel material for Dy(III) and its adsorption from wastewater.

Among different methods applied for removal of metal ions, such as adsorption, reverse osmosis, reduction, solvent extraction, coagulation, ion exchange, chemical precipitation, and membrane-based separation, adsorption is widely preferred because of simple instrumentation, ease of handling, versatility, cost effectivity, accuracy, and reusability of adsorbents.[28] In this context, adsorption of Dy(III) has been attempted through natural substances, such as activated carbon from waste coffee seeds,[2] microporous chitosan membrane,[10] charcoal,[29] and vermiculite;[8] nanocomposite;[9] and activated silica.[30] The natural adsorbents are inexpensive, but suffer from poor adsorption capacities, mechanical stabilities, and reusability. In contrast, the chemically modified inorganic materials possess better adsorption capacities and mechanical stabilities, but they are nonbiocompatible and costly. Therefore, there is a serious need of low-cost sustainable adsorbent which is mechanically stable, biocompatible, and can adsorb Dy(III) selectively and rapidly. At the same time, it can be recovered very easily. Recently, scalable-and-reusable hybrid composite materials are drawing much attention worldwide for sensing and recovery/removal of hazardous components, such as heavy and rare earth metal ions, dyes, and polyaromatics.[31−33] Multifunctional hydrogels are attracting much attention for sensing[34] and adsorbent for removing various metal ions.[35] Hydrogel is a 3D flexible porous polymer network with a soft and rubbery appearance that can uptake water several times that of its own weight. Swelling of these hydrogels is attributed to the varied ratio of hydrophilic-to-hydrophobic functionalities introduced by varying the synthesis conditions, such as temperature; pH; monomer ratio; and wt % of AGO, cross-linker, and initiators.[36] In this context, Mondal et al.[37,38] reported the in situ incorporation of O−C coupled third and fourth comonomers during free radical solution polymerization of two monomers. Mahapatra et al.[26] reported detection of Bi(III) using intrinsically fluorescent terpolymer hydrogels. Mondal et al.[32] observed the effect of multifunctional collagen dopants on the adsorption capacity toward Ti(IV), As(V), and V(V). They observed increased adsorption with increasing the dopant %. Therefore, dopants play an important role in elevating adsorption of metal ions. In order to utilize this concept, functionalized graphene can be considered as dopant because of the prevalent variegated covalently bonded functionalities containing oxygen, nitrogen, and sulfur.[39,40] The higher surface area to volume ratio and porous structure of 2D graphene is expected to facilitate the ionic/coordinative interaction with Dy(III). However, the availability of only oxygen-functionalities restricts its widespread applicability as sensor/adsorbent. Therefore, amine-functionalization of GO (i.e., AGO) can be an excellent alternative, since AGO contains a wide variety of functionalities, such as $-NH_2$, >NH, >N−, −CONH−, −CON<, and =C−N, in addition to −COOH, −OH, and >C=O of GO. These hydrophilic functionalities are expected to impart aqueous solubility, interfacial surface area-to-volume ratio, nontoxicity, biocompatibility, and mechanical properties.[41] Moreover, these nitrogenous functionalities can facilitate complexation of Dy(III) with the hydrogel resulting in the ease of fluorescence-based sensing and adsorption-based recovery of Dy(III). Despite having extraordinary capacitive properties, the direct use of AGO as sensor and adsorbent is limited due to its particulate nature. To the best of our knowledge, no amino graphene oxide-based hydrogel has been reported until date capable of *selectively* sensing Dy(III) at very low concentration along with the simultaneous adsorption of Dy(III). Also, the **AGO-EPH** designed in such a way that the adsorbed Dy(III) can be recovered very easily by simple pH reversal which is demonstrated by consecutive 5 adsorption−desorption cycles.

Present study describes (i) room temperature synthesis of the novel pH-responsive AGO-EPH from two nonfluorescent monomers via in situ incorporation of the third comonomer acting as the primary fluorophore; (ii) selective sensing of Dy(III) in nanomolar level with respect to other rare earth elements; (iii) coupled adsorption of Dy(III) alongside its sensing; (iv) desorption-based recovery of Dy(III) by simple pH reversal; and also (v) AGO-EPH shows inherent antibacterial properties.

Herein, an intrinsically fluorescent purely aliphatic AGO-EPH hydrogel is synthesized from two nonfluorescent hydrophilic monomers, such as PNA and PEAM, along with the in situ incorporation of a new N−C coupled comonomer, AAPPA, via simple free radical solution polymerization. First, GO is synthesized from graphite powder using the modified Hummers method, and then converted into AGO through the one-pot solvothermal technique. Subsequently, poly[PNA-*co*-PEAM] hydrogels is synthesized, followed by incorporation of AGO with the optimal reaction mixtures for synthesize of AGO-EPH. The hydrogels are characterized in details using NMR, FTIR, XRD, TEM, SEM, EDX, Raman, MALDI-mass, DLS, and UV−visible studies. The fluorescent properties of AGO-EPH are determined and its selective turn-off sensing toward Dy (III) is demonstrated. Adsorption studies are conducted using simulated solutions containing Dy(III) in the concentration range of 5−30 mg/L at pH_w = 7 and ambient temperature. The equilibrium adsorption data are fitted to different isotherm and kinetic models to determine various

https://doi.org/10.1021/acsomega.4c02772
ACS Omega 2024, 9, 29620−29632

Scheme 1. Synthesis of EPH from Ex Situ Added Monomers/Crosslinker and In Situ Strategic Incorporation of the Third Comonomer

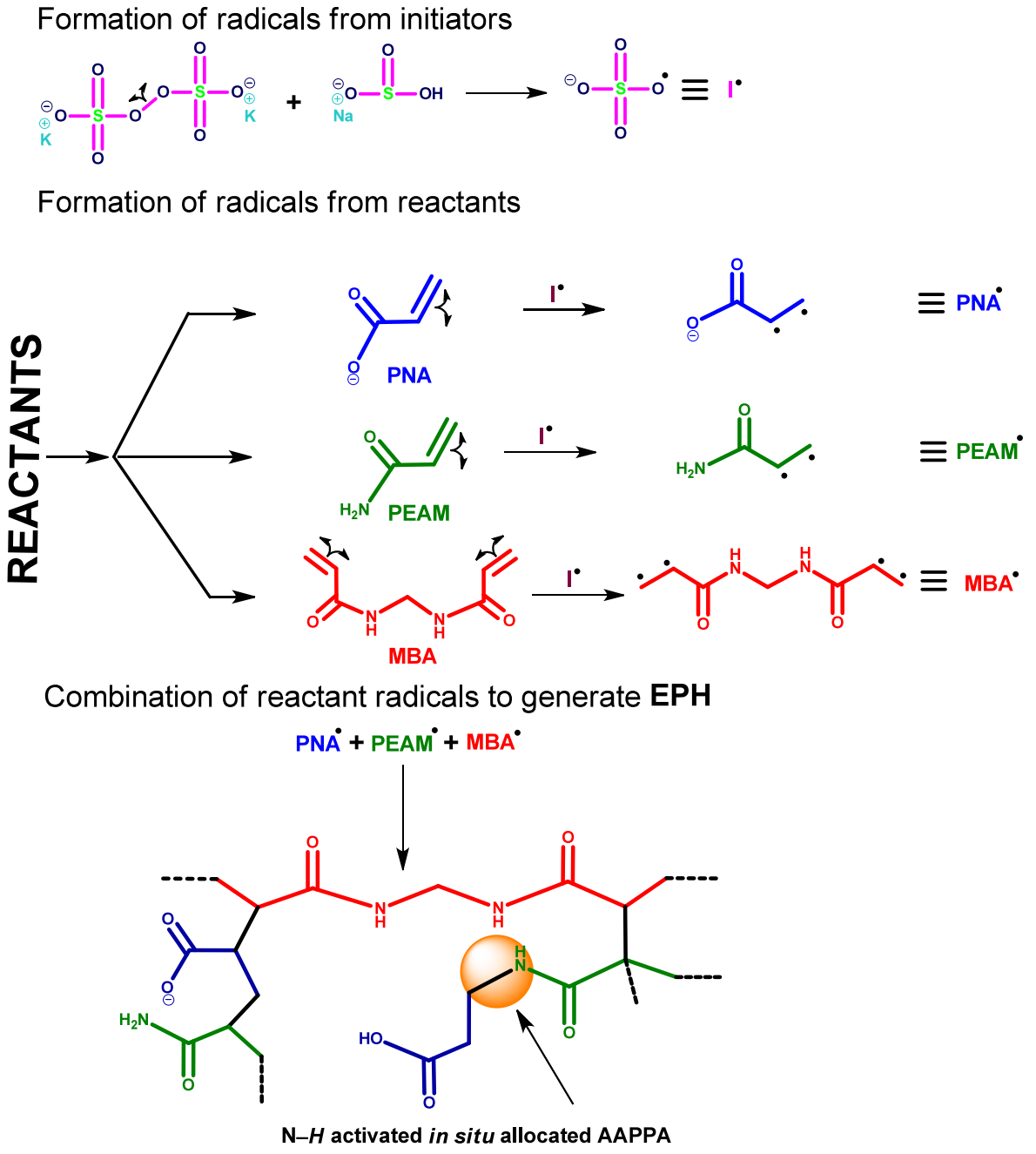

parameters. The desorption (recovery) studies are conducted using five consecutive adsorption−desorption studies by regulating the pH in the range of 2−7. Finally, the antibacterial property is demonstrated using *E. coli* bacteria for safe disposal of the materials.

2. EXPERIMENTAL SECTION

2.1. Materials. PNA, PEAM, graphite powder, *N*,*N*′-methylenebis(acrylamide) (MBA), DMSO, $NaHSO_3$, $K_2S_2O_8$, and $Dy(NO_3)_3$ were purchased formed Sigma-Aldrich and used without any modification/purification. The entire experiments were carried out by using milli-Q-water.

2.2. Synthetic Methodology. *2.2.1. Synthesis of GO from Graphite Powder.* Herein, GO was synthesized from graphite powder using the modified Hummers method.[42] In brief, to the 30 mL mixture of concentrated H_2SO_4 and H_3PO_4 (3:1 v/v), 2.25 g of oven-dried graphite powder was added slowly with constant stirring at 300 rpm at 27 °C. Thereafter, 13.20 g of solid $KMnO_4$ was added slowly into the mixture to initiate oxidation of graphite. The isothermal stirring was continued until the solution became dark green, followed by dropwise addition of 50 mL of 10 vol % H_2O_2 solution to remove the excess $KMnO_4$. Since this step is exothermic, it was carried out in cold water-bath to maintain the constant temperature at 27 °C. Then the mixture was stirred for 30 min, GO was separated by centrifugation, washed thoroughly, and dried in vacuum oven.

https://doi.org/10.1021/acsomega.4c02772
ACS Omega 2024, 9, 29620−29632

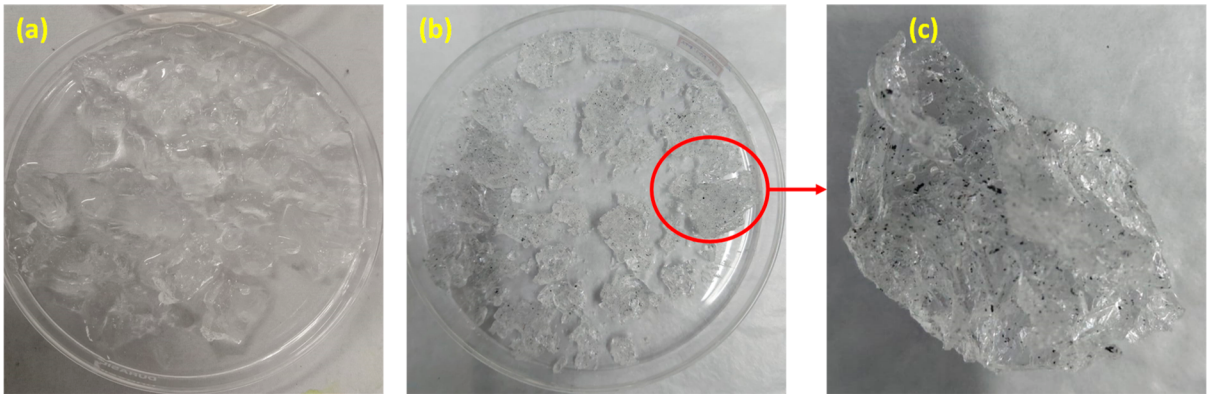

Figure 1. Optical images of (a) **EPH**, (b) **AGO-EPH**, and (c) zoomed **AGO-EPH** [Photograph courtesy of Mrinmoy Karmakar. Copyright 2024].

2.2.2. Synthesis of AGO from As-Synthesized GO. The as-obtained GO was converted to AGO by using the solvothermal one-pot technique.[43] In brief, 0.16 g of the previously synthesized GO was sonicated with 20 mL of milli-Q-water for 30 min to obtain a homogeneous suspension, which was then put into a 100 mL Teflon-lined autoclave. After that, 70 mL of 25 vol % ammonia solution was added to the autoclave, and heated at 200 °C for 12 h. The leftover ammonia solution was rinsed off by using 0.5 [M] HCl solution, and then the solid was washed repeatedly with milli-Q-water. The final product, i.e., AGO, was obtained by centrifugation, washed again, and dried in vacuum.

*2.2.3. Synthesis of Engineered Polymer Hydrogel (**EPH**).* A series of poly[PNA-*co*-PEAM] hydrogels were synthesized by varying synthesis parameters, such as PNA:PEAM (−/ *A*); amounts cross-linker (wt %/ *B*), initiators (wt %/ *C*), and total monomers (wt %/ *D*); and temperature (K/ *E*) within 5−15; 1.0−2.0, 1.0−2.5, and 10−30 wt %; and 290−310 K, respectively (Table S1 of the Supporting Information, SI). Since network integrity, swelling properties, and reusability of hydrogel severely depend on the variation of synthesis parameters, optimization of these parameters is essential to obtain the optimum hydrogel. Herein, the optimum conditions were achieved at: 10, 2.0 wt %, 1.5 wt %, 20 wt %, and 300 K for *A*, *B*, *C*, *D*, and *E*, respectively. To synthesize the optimum **EPH** (Scheme 1), 4.551 g dry PNA was taken in a 100 mL stoppered conical flask, dissolved in 12.8 mL of milli-Q-water, and neutralized to pH = 5.5 by using 2.2 mL of the saturated NaOH solution. To this solution, 0.449 and 0.5 g of PEAM and MBA, respectively, were added and homogenized under constant stirring at 600 rpm and 300 K for 2 h. After that, N_2-gas purged to this homogeneous solution and polymerization was initiated by adding redox initiators (0.15 g each of $NaHSO_3$ and $K_2S_2O_8$ dissolved in 5 mL water). Gelation was observed at 32 min. The as-obtained **EPH** was collected from conical flask (Figure 1a), washed with 1:1 (v/v) water/methanol solution, and dried in hot-air oven for 48 h.

*2.2.4. Synthesis of **AGO-EPH**.* Like **EPH**, for synthesizing the optimum **AGO-EPH** (Table S1), 4.551 g dry PNA was taken in a 100 mL stoppered conical flask, dissolved in 12.8 mL of milli-Q-water, and neutralized to pH = 5.5 by using 2.2 mL of the saturated NaOH solution. After adding 0.449 and 0.5 g of PEAM and MBA, respectively, to this solution, 0.2 g AGO added to the resultant mixture, and homogenized at 300 K for 3 h. After that, polymerization was initiated by adding redox initiators (0.15 g each of $NaHSO_3$ and K_2S2O_8 dissolved in 5 mL water) in N_2-environment. This time gelation took longer time of 180 min. The as-obtained **AGO-EPH** was collected from conical flask (Figure 1 b,c), washed with 1:1 (v/v) water/methanol solution, and dried in a hot-air oven for 48 h.

2.3. Characterization. Structures of **EPH**, **AGO-EPH**, and Dy(III)-**AGO-EPH** were characterized by ^{1}H NMR (Ascend NMR-500 MHz, Bruker), FTIR (Spectrum-2, Singapore, PerkinElmer), TG (TGA 4000, PerkinElmer), XRD (D8 Discover, Bruker), FESEM/EDX (JSM7600F, Jeol), DLS (Nano ZS, Malvern Instruments), and UV−vis (Specord 210 Plus, AnalytikJena) analyses. Chemical structures; graphs; and TOC graphic were generated by ChemDraw Ultra 12.0; Origin 9.0; and Adobe Illustrator 2023 (version 27.0.1), Photoshop Desktop (version 25.0), and Freepik software, respectively.

2.4. Fluorescence Intensity Measurement of AGO-EPH. Herein, 50 mg of dried and crushed **AGO-EPH** was sonicated with 50 mL DMSO to obtain a homogeneous hydrogel solution. The UV−vis spectrum of this hydrogel solution was recorded to obtain the λ_{max}. Thereafter, fluorescence emission experiment (Horiba Fluorolog-3 modular spectrofluorometer) was carried by considering the same λ_{max} as the excitation wavelength.

2.5. Adsorption Methodology. Isothermal adsorption experiments were conducted by dipping 0.025 g of dry **AGO-EPH** within 50 mL Dy(III) solution within 5−30 mg L^{-1} at pH_w = 7. Adsorption isotherm and kinetics data were determined by measuring unadsorbed Dy(III)-concentrations (mg L^{-1}) at different time intervals by ICP-MS. The equilibrium ACs (mg g^{-1}), rate constants, and thermodynamics parameters were estimated by methods reported elsewhere.[44] Briefly, the equilibrium isothermal adsorption data were fitted to several isotherm models, such as Langmuir, Freundlich, BET, Sips, and Henry isotherm models (eqs 1−5).

$$q_e = q_{max}\frac{k_L C_e}{1 + k_L C_e} \quad (1)$$

$$q_e = k_H C_e \quad (2)$$

$$q_e = k_F C_e^{1/n} \quad (3)$$

$$q_e = q_{max}\frac{(k_S C_e)^{\gamma}}{1 + (k_S C_e)^{\gamma}} \quad (4)$$

$$q_e = q_{BET}\frac{k_1 C_e}{(1 - k_2 C_e)(1 - k_2 C_e + k_1 C_e)} \quad (5)$$

https://doi.org/10.1021/acsomega.4c02772
ACS Omega 2024, 9, 29620−29632

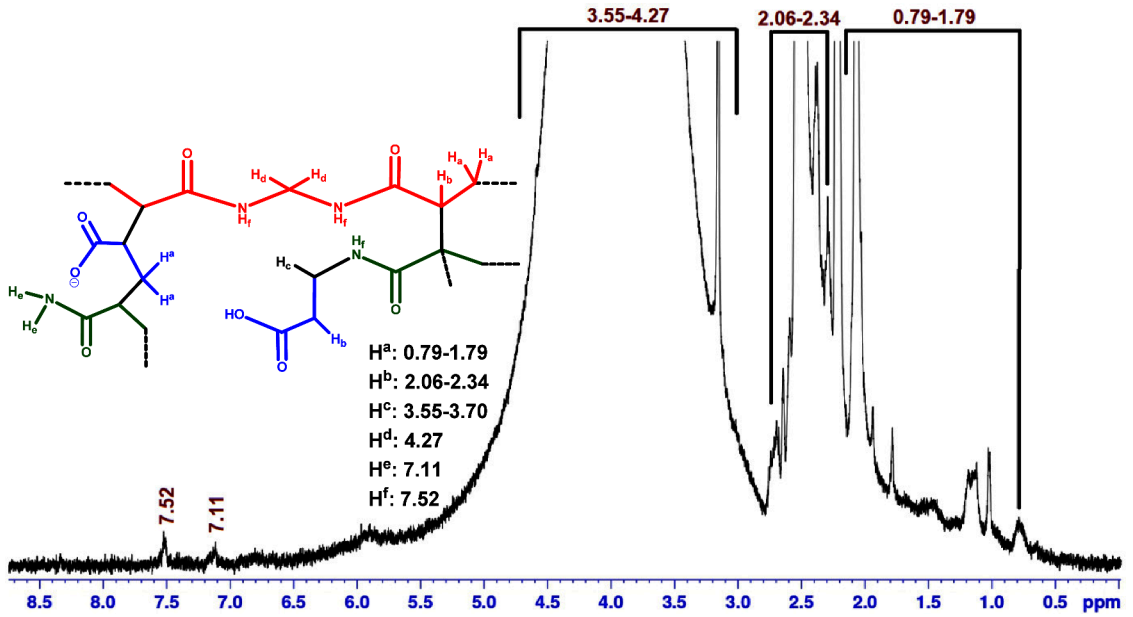

Figure 2. ^{1}H NMR analysis of **EPH**.

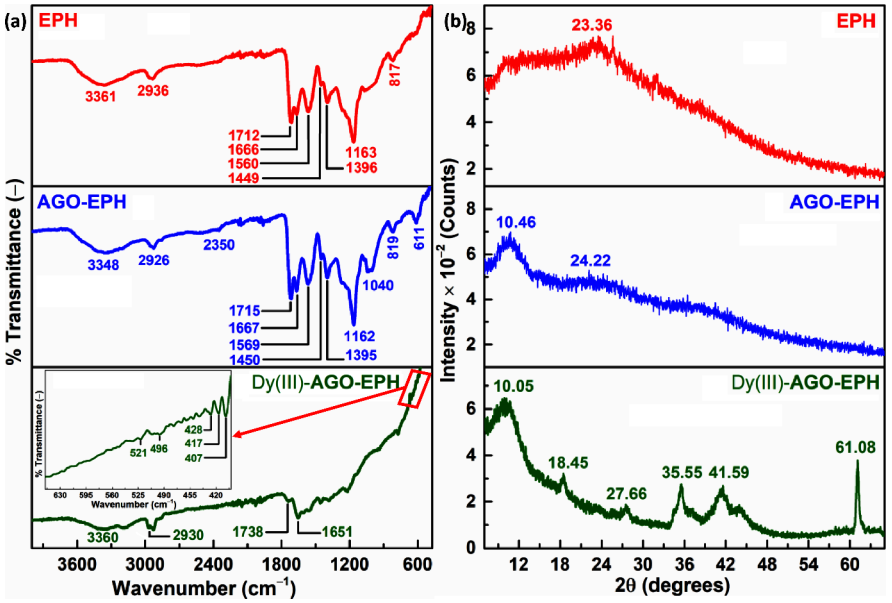

Figure 3. (a) FTIR and (b) XRD analyses of **EPH**/**AGO-EPH**/Dy(III)-**AGO-EPH**.

Here, q_e, C_e, and $n/q_{BET}/\gamma$ represent adsorption capacity, residual Dy(III)-concentration at equilibrium, and Freundlich/BET/Sips parameters, respectively. k_F, k_1/ k_2, k_S, k_H, and k_L are Freundlich, BET, Sips, Henry, and Langmuir isotherm constants, respectively.[45]

2.6. Desorption and Reusability Studies of AGO-EPH. Desorption of the adsorbed Dy(III) is important to reuse it for the high-value industrial applications. Since Dy(III) adsorption was carried out at $pH_w > pH_{PZC}$, desorption of Dy(III) from Dy(III)-**AGO-EPH** was strategically performed at $pH_w < pH_{PZC}$. Thereafter, the recovered **AGO-EPH** was deployed further for adsorption at $pH_w = 7$, and again desorption was tried at $pH_w = 2$. Such replicate adsorption−desorption experiments were studied for 5 cycles to obtain free Dy(III) and confirm the reusability of **AGO-EPH**.

3. RESULTS AND DISCUSSION

3.1. Characterization of Graphite, GO, and AGO. *3.1.1. Raman Spectroscopic Analysis.* In the Raman spectrum of graphite, the intense D-/G-bands at 1349/1570 cm^{-1} and the broad 2D-band at 2693 cm^{-1} (Figure S1a) indicates the existence of multiple disorders in the structure of the used graphite. Moreover, the I_D/I_G ratio of 0.54 confirms the existence of three layers[46] in the structure of used graphite. In GO, shifting of D- and G-bands to 1336 and 1577 cm^{-1}, respectively, and simultaneous broadening of these bands confirm transformation of sp^2 carbon of graphite to sp^3 in GO.[47] In AGO, grafting of various *N*-containing functionalities, such as −NH$_2$, >NH, >N−, −CONH−, and −CON<, is indicated by further shifting of D-band to 1340 cm^{-1} in AGO.

https://doi.org/10.1021/acsomega.4c02772
ACS Omega 2024, 9, 29620−29632

3.1.2. XRD Analysis. In the XRD image of graphite (Figure S1b), the sharp peak at 2θ = 26.64° with *d*-spacing of 3.35 Å indicates the presence of (002) plane of hexagonal graphitic planes.[48] After exfoliation by H_2SO_4, this peak disappears and a new sharp peak appears at 2θ = 26.64° with the *d*-spacing of 8.42 Å because of the (001) plane. The appearance of this peak and increasing in *d*-spacing confirm the addition of oxygen during chemical exfoliation of graphite to generate hydroxyl, epoxy, and carbonyl functionalities. In fact, the *d*-spacing of this peak increases further to 8.56 Å after amination, inferring the functionalization of GO-surface by $-NH_2$ groups.[48] Moreover, in AGO, peaks at 2θ = 10.46°, 16.11°, and 21.91° indicate the presence of −CONH− and −CON<.[49]

3.1.3. FESEM, EDX, and TEM Analysis. The FESEM and TEM images (Figure S2a,d) of graphite contain layered structure, similar to the observation from Raman spectrum (Figure S1a). In GO, the effect of exfoliation on the layers is very prominent and hence distinct planes are visible from both FESEM and TEM images (Figure S2b,e). In fact, FESEM image of GO is very much like that reported by Aliyev et al.[50]

From FESEM image of AGO (Figure S2c), the planar structure is found to be modified significantly leaving behind the flaky-type appearance,[51] whereas in TEM image (Figure S2f), agglomeration is observed. The generation of extensive hydrogen bonding because of the excessive hydrophilic *N*-containing functionalities causes such a superficial feature. From EDX spectrum of graphite (Figure S3a), only the peak of carbon can be visualized, whereas in GO (Figure S3b), peaks of carbon and oxygen are present. The introduction of *N*-containing functionalities in AGO is further confirmed from the appearance of nitrogen peak in EDX spectrum of AGO (Figure S3c), which is absent in graphite and GO.

3.2. Characterization of EPH and AGO-EPH. In **EPH**, C−C coupled formation of saturated moieties, such as $-\mathbf{H}_2C-$ and >C**H**− from $H_2C{=}CH-$ of PNA/PEAM/MBA is confirmed from $-C\mathbf{H}_2-$ and >C**H**− peaks within 0.79−1.79 and 2.06−2.34 ppm, respectively (Figure 2), substantiated by C−C/C−H peaks of − $H_2C-CH<$ at 1163/2936 and 1162/2926 cm^{-1} (Figure 3a) in **EPH** and **AGO-EPH**, respectively. In fact, the completion in polymerization is further confirmed through the absence of $\mathbf{H}_2C{=}C\mathbf{H}-$ peaks within 6.03−6.59, 5.70−6.30, and 5.59−6.13 ppm for PNA, PEAM, and MBA,[52] respectively, and C−H *def.* and *overtone* peaks of $H_2C{=}CH-$ at 980 and 1830 cm^{-1}, respectively. The incorporation of PEAM and MBA in **EPH** can be inferred from the characteristic $-N\mathbf{H}_2$ and $-CO-N\mathbf{H}-CH_2-N\mathbf{H}-CO-/-CO-NH-C\mathbf{H}_2-NH-CO-$ peaks at 7.11 and 7.52/4.27 ppm, respectively, substantiated from FTIR peaks at 1666/1667, 1396/1395, and 817/819 of >C=O *str.* (amide-I), C−N *str.* (amide-III), and N−H *wagging* (amide-V) of primary amide, respectively, in **EPH**/ **AGO-EPH**. The incorporation of PNA in **EPH** and **AGO-EPH** is confirmed from >C=O *str.* peaks of −COOH dimer at 1712 and 1715 cm^{-1}, respectively. Importantly, generation of the third comonomer, i.e., AAPPA, via in situ N−*H* activation can be inferred from the arrival of the new characteristic $-CO-NH-CH_2-CH_2-$ peak within 3.55−3.70 ppm in **EPH**, substantiated from N−H *bending* (amide-II) and C−N *str.* (amide-III) of secondary amide at 1560/1569 and 1449/1450 cm^{-1}, respectively, in **EPH**/ **AGO-EPH**.[53] In **AGO-EPH**, the greater population of $-NH_2$ functionalities from AGO than that of **EPH** can be ascertained from the bathochromic shifting of hydrogen bonded O−H··· N−H *str.* from 3361 cm^{-1} of **EPH** to 3348 cm^{-1} in **AGO-EPH** and arrival of C−N *str.* and strong hydrogen bonded O−H··· N−H *str.* at 1040 and 2350 cm^{-1} in **AGO-EPH**, substantiated from the delayed release of H_2O up to 200 °C (Figure 4),

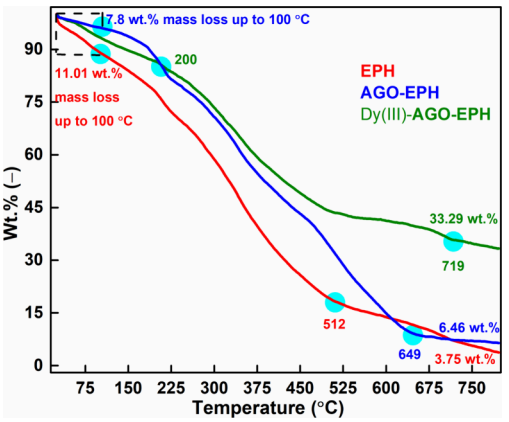

Figure 4. TG analyses of **EPH**/**AGO-EPH**/Dy(III)-**AGO-EPH**.

elevated overall thermal stability of **AGO-EPH** compared to **EPH**, and the significant increase in the final decomposition temperature of **AGO-EPH** (649 °C) than that of **EPH** (512 °C). Moreover, the presence of AGO in **AGO-EPH** can be inferred by the appearance of a new peak at 611 cm^{-1} because of C=C *bending* of AGO, shifting of XRD peak from 2θ = 23.36° of **EPH** to 2θ = 24.22° in **AGO-EPH**, and appearance of a new XRD peak at 2θ = 10.46° (Figure 3b), which exactly matches with the (001) plane of AGO. The FESEM images of **EPH** contains featureless homogeneous morphology (Figure 5a,b), whereas the **AGO-EPH** surface endows the distinct phase boundaries of AGO and polymer matrix (Figure 5c). Moreover, in the higher magnification FESEM image (Figure 5d) of **AGO-EPH**, agglomerated flaky particles of AGO can be seen. The presence of AGO in **AGO-EPH** is further substantiated from MALDI-TOFF mass spectrometric analyses, where only single signal is observed at m/z = 3877.87 in **EPH** (Figure S4), whereas three signals are prominent at m/z = 3873.59, 4437.40, and 4821.87 for **AGO-EPH**. The increase in hydrodynamic radius from 251 nm (Figure 6a) of **EPH** to 365 nm (Figure 6b) in **AGO-EPH** harmonized the presence of AGO in **AGO-EPH**.

3.3. Characterization of Dy Adsorbed AGO-EPH (Dy(III)-AGO-EPH). Substantial alteration can be observed in the characteristic features of **AGO-EPH** after Dy(III) adsorption. Since Dy(III)-adsorption has been carried out at $pH_w > pH_{PZC}$ (pH_{PZC} = 6.28, Figure S5), most of the −COOH/O−H is converted to $-COO^-/-O^-$, resulting in the rapid degradation of hydrogen bonding moieties in Dy(III)-**AGO-EPH**.[54−56] Such phenomenon is linked with the broadening and weakening of hydrogen bonded O−H··· N−H *str.* at 3374 cm^{-1} (Figure 3a) in Dy(III)-**AGO-EPH**, shifting of >C=O *str.* of −COOH dimer from 1715 cm^{-1} in **AGO-EPH** to 1738 cm^{-1} in Dy(III)-**AGO-EPH**, and the inferior thermal stability of Dy(III)-**AGO-EPH** than that of **AGO-EPH** up to 200 °C (Figure 4). After Dy(III) adsorption, the rapid reduction of the intensities of >C=O *str.* of $-COO^-$ and $-CONH_2$ (at 1738 and 1651 cm^{-1}, respectively) envisaged the participation of >C=O in coordination with Dy(III). The appearance of low intensity peaks at 407, 417, 428, 496, and 521 cm^{-1} in Dy(III)-**AGO-EPH** is attributed to Dy−O bond, formed via coordinating interaction [$-COO^-$ →

https://doi.org/10.1021/acsomega.4c02772
ACS Omega 2024, 9, 29620−29632

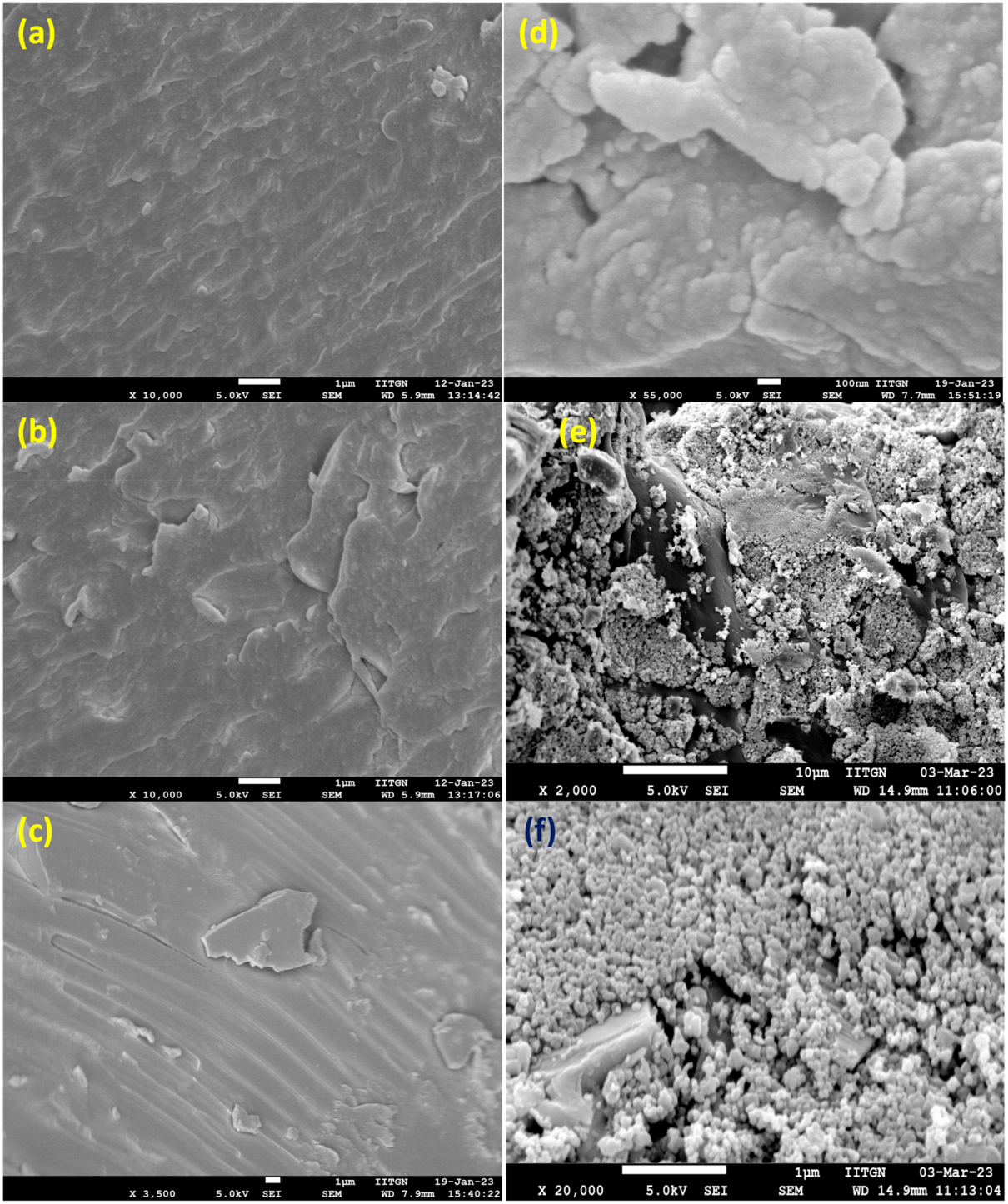

Figure 5. FESEM images of (a/b) **EPH**, (c/d) **AGO-EPH**, and (e/f) Dy(III)-**AGO-EPH** in high/low magnifications.

Dy(III)] between $-COO^-$ of **AGO-EPH** and Dy(III) during adsorption at $pH_w > pH_{PZC}$.[57] Such strong coordination can also be confirmed from the elevated thermal stability of Dy(III)-**AGO-EPH** with respect to **AGO-EPH** beyond 200 °C, significantly higher residue content of 33.29 wt.% compared to 6.49 wt.% of **AGO-EPH**, and appearance of Dy(III)-specific XRD peaks at 2θ = 18.45°, 27.66°, 35.55°, 41.59°, and 61.08° (Figure 3b).[57] The superficial deposition of Dy(III)-crystals are visible from the FESEM images of Dy(III)-**AGO-EPH** (Figure 5e,f).

3.4. Fluorescence-Based Sensing of Dy(III) by AGO-EPH. The as-synthesized **AGO-EPH** exhibits blue fluorescence (Figure 7e), whereas the monomers, cross-linker, and AGO are nonfluorescent. Herein, another AGO-based hydrogel has been synthesized by using the lower initiator amount. This copolymeric hydrogel has no fluorescence property. Therefore, the N−H activated incorporated new comonomer, i.e., AAPPA, can be considered as the fluorophore in **AGO-EPH**. From UV−vis plot (Figure 7a) of DMSO-solution of **AGO-EPH**, the λ_{max} is found to be 268 nm. Therefore, the fluorescence emission spectrum of **AGO-EPH** is studied by

https://doi.org/10.1021/acsomega.4c02772
ACS Omega 2024, 9, 29620−29632

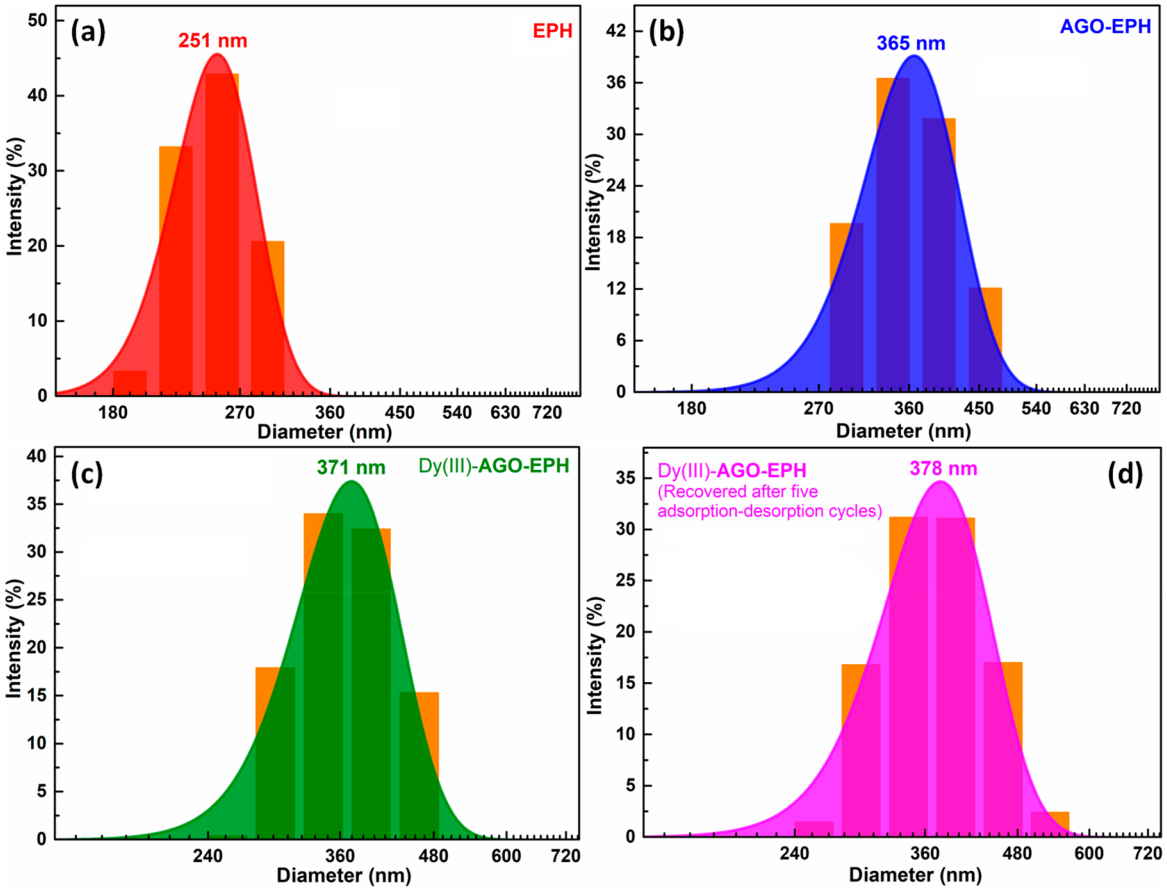

Figure 6. DLS analyses of (a) **EPH**, (b) **AGO-EPH**, (c) Dy(III)-**AGO-EPH**, and (d) Dy(III)-**AGO-EPH** recovered after five complete adsorption−desorption cycles.

exciting hydrogel solution at 268 nm. From the emission plot, two distinct fluorescence bands at 412 and 440 nm (Figure 7b) are observed for **AGO-EPH**. However, the fluorescence intensity is found to be quenched rapidly with the gradual addition of Dy(III) (Figure 7d). In order to observe the *selectivity* of metal ion sensing, 58.06×10^{-5} (M) solutions of a few rare metal ions, such as Dy(III), Eu(III), Sm(III), Yb(III), Gd(III), Ce(III), Nd(III), and Pr(III), were added in different DMSO-solutions of **AGO-EPH**, followed by measuring their emission intensities at the same excitation wavelength of 268 nm. From these emission spectra (Figure 7c), the relative intensity (I/I_0) of **AGO-EPH** is found to reduce significantly only after Dy(III) addition, whereas for all other REMs, the I/I_0 values remain mostly unaltered with respect to the control study. Therefore, the *selective* Dy(III) sensing with respect to other REMs can be inferred. Importantly, the LOD of Dy(III) sensor is found to be as low as 1.88×10^{-7} (M) (Figure S6), which is lower than those of 1.02×10^{-5} and 1.00×10^{-7} (M), reported by Chen et al.[15] and Jianjun et al.,[27] respectively.

3.5. Logic Gate Estimation. To understand the underlying mechanism of fluorescence quenching of **AGO-EPH** after adsorption of Dy(III), the EDTA-based complexation concept is utilized. Herein, if the polymer-EDTA complex exhibits similar fluorescence intensity that signifies no interaction between the fluorescent **AGO-EPH** and nonfluorescent EDTA. However, during the experiment the fluorescence quenching of Dy(III)-**AGO-EPH** is observed in the presence of EDTA solution. This implicates formation of Dy(III) and **AGO-EPH** complex (Dy(III)-**AGO-EPH**). Since, EDTA is a stronger chelating ligand than that of **AGO-EPH**, it binds with Dy(III) stronger than that of **AGO-EPH**, leaving free **AGO-EPH** and turn off the sensing. The entire study can be summarized through the following truth tables and logic gate (Scheme 2).

3.6. Adsorption of Dy(III) by AGO-EPH. During isothermal adsorption experiments, the higher rate of adsorption is observed at the beginning because of the availability of the larger amount of vacant adsorption cites. With the progress of adsorption, the rate of adsorption is decreased gradually to attain equilibrium. The equilibrium adsorption data are fitted to different isotherm models, such as such as Langmuir, Henry, Freundlich, Sips, and BET,[58,59] of which Langmuir model shows the best fit because of the highest adjusted R^2/F and lowest χ^2 values.[58] The maximum AC, i.e., q_{max}, is found to be 42.09, 38.97, 36.53, and 34.27 mg g^{-1} at 298, 303, 308, and 313 K (Figure 8a and Table 1), respectively. Again, the better fitting of kinetics data with pseudo-second-order kinetics model compared to pseudo-first-order kinetics model (Figure 8b) and attainment of the activation energy of 70.03 kJ mol^{-1} (Figure 8d) confirm chemisorption of Dy(III) by **AGO-EPH**.[60,61] The presence of $-COO^-/-CONH_2/-CONH^-$ functionalities from **EPH** and $-NH_2/-NH-$ of AGO were involved in chemical bonding with Dy(III), as observed earlier from material characterization data. The k_2 values are found to increase with the increase in temperature, confirming the faster adsorption at higher temperatures. The exothermic spontaneous nature of chemisorption can be understood from the negative values of ΔH^0

https://doi.org/10.1021/acsomega.4c02772
ACS Omega 2024, 9, 29620−29632

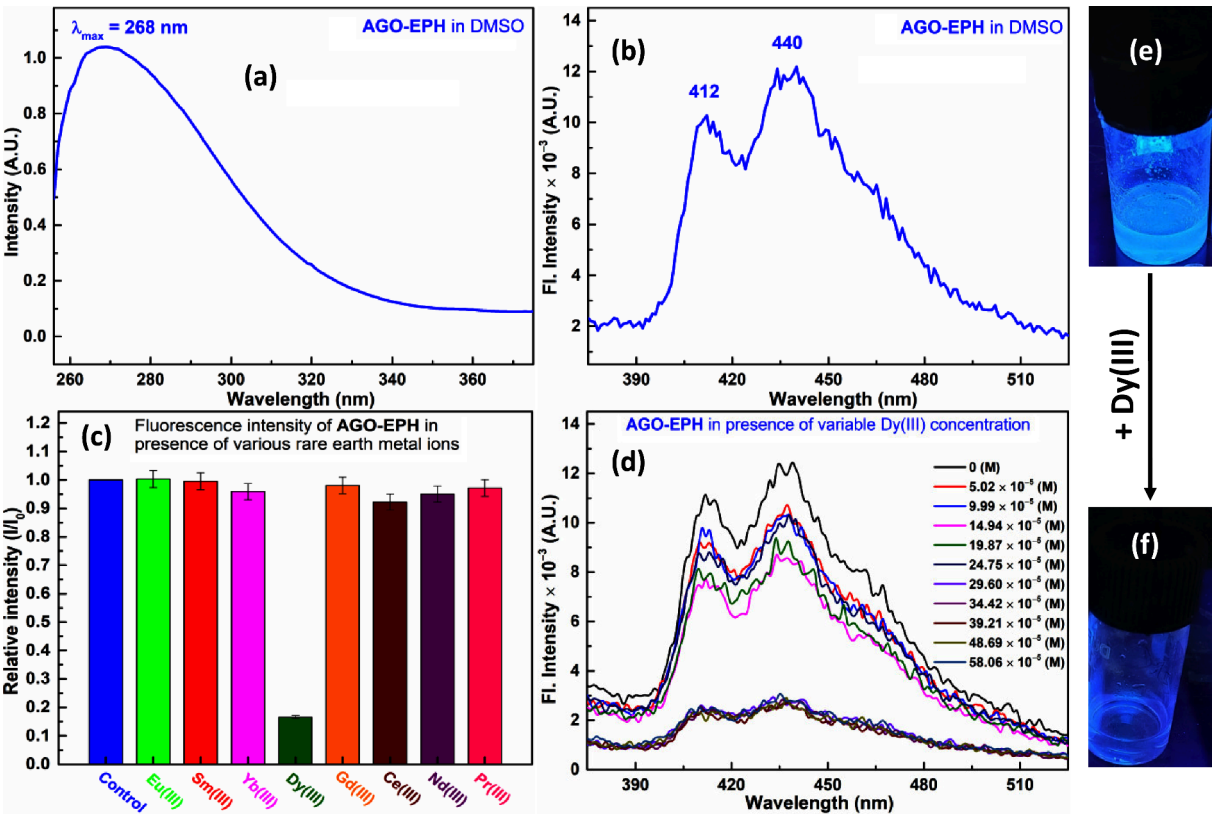

Figure 7. (a) UV−vis and (b) fluorescence emission spectra ($\lambda_{excitation}$ = 268 nm) of **AGO-EPH** in DMSO solvent, (c) relative intensities of **AGO-EPH** in-presence of different rare metal ions, (d) quenching of fluorescence intensity of **AGO-EPH** after adding varying concentrations of Dy(III) solutions, and (e/f) UV-images of DMSO solutions of **AGO-EPH**/ Dy(III)-**AGO-EPH** [Photograph courtesy of Mrinmoy Karmakar. Copyright 2024].

Scheme 2. Truth Table and Logic Gate to Explain the Fluorescence Quenching of Dy(III) by AGO-EPH

Inputs		Output
Dy(III)	EDTA	
0	0	1
1	0	0
0	1	1
1	1	1

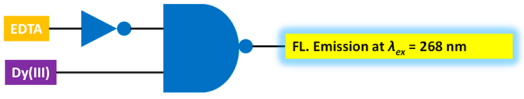

and ΔG^0 at the entire working temperature (Figure 8c and Table 2).

3.7. Desorption of Dy(III) from Dy(III)-AGO-EPH and Reusability Studies of AGO-EPH. Herein, adsorption and desorption Dy(III) are achieved by introducing electrostatic attraction and repulsion of Dy(III) with anionic and cationic surfaces of **AGO-EPH**, respectively, by varying the working pH. The % adsorption/% desorption varies as 98.21/92.17, 94.05/93.22, 92.76/94.89, 90.07/95.97, 80.06/97.22, and 65.06/97.31%, respectively, for 1−6 cycles (Figure 9). With the increase in adsorption−desorption cycles, the network integrity kept on reducing, leading to the reduced %adsorption. These data clearly indicate that the same **AGO-EPH** can be used for adsorbing Dy(III) for at least 5 times (as % adsorption of sixth cycle is very low, and hence reusability of the adsorbent is reported up to fifth cycle only). Moreover, the structural integrity is investigated by measuring hydrodynamic radii of **AGO-EPH**, i.e., R_{hyd}, and **AGO-EPH** desorbed after sixth cycle, i.e., R_{hyd}',[33] in which the closeness of R_{hyd} (371 nm) and R_{hyd}' (378 nm) (Figure 6c,d) confirmed significant retention of **AGO-EPH** network.

3.8. Antibacterial Property. The antibacterial properties of **EPH** and **AGO-EPH** are studied against 200 μL of ∼3 × 10^8 cells mL^{-1} solutions of Gram-negative *E. coli* bacteria. **AGO-EPH** is found to possess the stronger antibacterial property (average DIZ = 7.73 mm) compared to **EPH** (Figure S7a). Moreover, from MTT assay test, the cytotoxicity of **AGO-EPH** is found to be lower than that of **EPH** (Figure S7b). From these data, it can be easily concluded that **AGO-EPH** is biocompatible and harmless to the environment as well as possesses antibacterial properties. Therefore, after sensing and 5 cycles of adsorption−desorption, **AGO-EPH** can be safely disposed of since it can still exhibit antibacterial properties.

4. CONCLUSIONS

The present work presents a design-and-synthesis route of intrinsically fluorescent multifunctional stable hydrogel, i.e., **AGO-EPH**, via entrapment of particulate AGO within the network of the optimum **EPH**, prepared from nonfluorescent PNA and PEAM monomers and N−*H* activated in situ attachment of the third comonomer, AAPPA. Internalization of particulate AGO in the optimized **EPH** improves the network

https://doi.org/10.1021/acsomega.4c02772
ACS Omega 2024, 9, 29620−29632

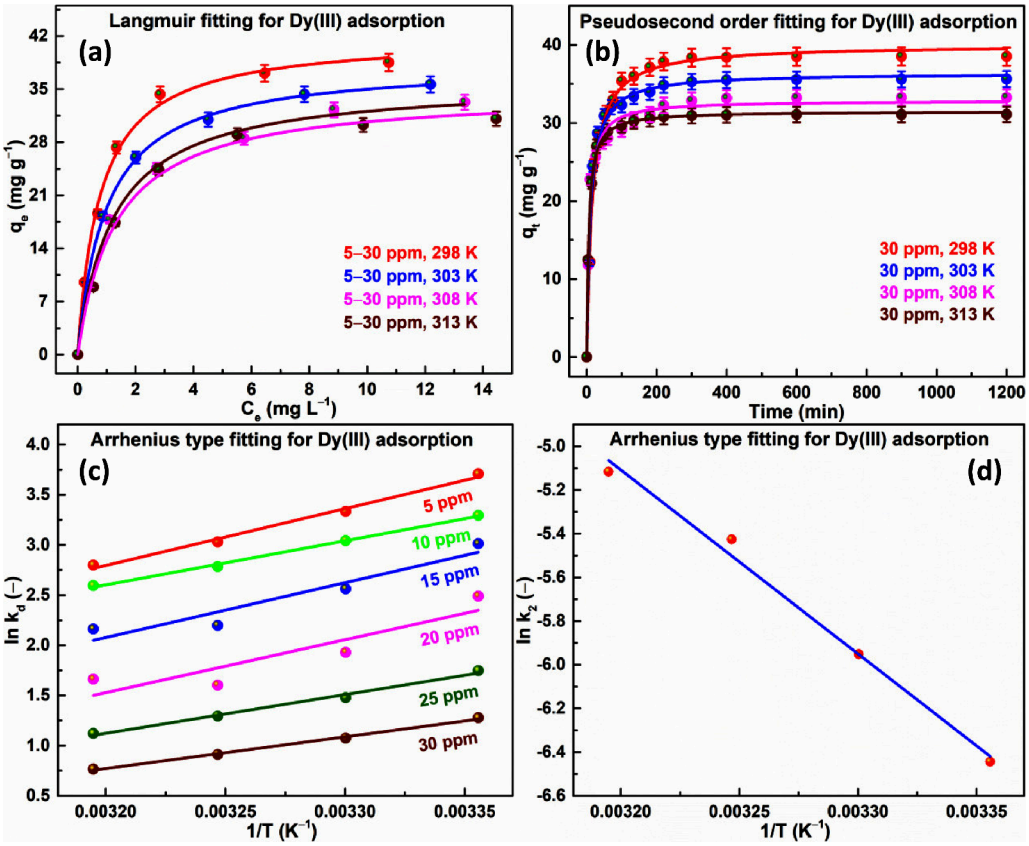

Figure 8. Adsorption (a) isotherm, (b) kinetics, and (c/d) thermodynamics fitting for Dy(III)-**AGO-EPH**.

Table 1. Adsorption Isotherm and Kinetics Parameters

	temperature (K)			
model/parameters	298	303	308	313
	Dy(III)-**AGO-EPH**			
Langmuir				
q_{max} (mg g^{-1})/ pH$_i$/ C_0 (mg L^{-1})	**42.09**/ 7/5–30	38.97/7/ 5–30	36.53/7/ 5–30	34.27/7/ 5–30
k_L (L mg^{-1})	1.3319	1.0307	0.8217	0.7709
R^2/ F	0.9968/3224.79	0.9994/20097.36	0.9972/7652.65	0.9955/3263.61
χ^2	0.8028	0.0997	0.3937	0.6437
Pseudo-second-order				
$q_{e,cal}$ (mg g^{-1})/pH$_i$/C_0 (mg L^{-1})	40.17/7/30	36.53/7/30	32.78/7/30	31.67/7/30
$q_{e,exp}$ (mg g^{-1})	38.23 ± 0.38	35.11 ± 0.39	33.43 ± 0.31	31.70 ± 0.29
k_2 (g mg^{-1} min^{-1})	0.0015	0.0026	0.0044	0.0056
R^2/ F	0.9905/7501.01	0.9903/7301.59	0.9829/4258.78	0.9988/60389.96
χ^2	1.0224	1.1129	1.7021	0.0901

stability, thermostability, hydrophilicity, functionality, reusability, antibacterial activity, and cell viability. The N–*H* activated in situ attachment of AAPPA is inferred by ^{1}H NMR peak within 3.55–3.70 along with N–H *bending* (amide-II) and C–N *str.* (amide-III) of secondary amide at 1560/1569 and 1449/1450 cm^{-1}, respectively, in **EPH**/ **AGO-EPH**. Adsorption of Dy(III) is occurred via coordinating interaction between >C═O of −COO$^-$/−CONH$_2$ of **AGO-EPH** and Dy(III) is confirmed by the occurrence of Dy–O type linkage in Dy(III)-**AGO-EPH**. The **AGO-EPH** is found to emit blue fluorescence and possess selective quenching for Dy(III) with respect to other rare metal ions, and the LOD is found to be as low as 188 nM. The in situ incorporated AAPPA comonomer is found to be the fluorophore of **AGO-EPH**. This hydrogel is found to absorb high % of Dy (III) over multiple cycles pH = 7 and also shown higher % of recovery (>90% of Dy (III) simply be changing the pH). The maximum adsorption capacity of **AGO-EPH** is 41.97 ± 0.39 mg g^{-1}. Moreover, **AGO-EPH** exhibits strong antibacterial property against Gram-negative *E. coli* bacteria with the average DIZ of 7.73 mm and very low cytotoxicity. From logic gate measurements by EDTA, complexation of Dy(III) and −COO$^-$ of **AGO-EPH** is established as the mechanism of fluorescence quenching. Overall, this environment-friendly multifunctional hybrid hydrogel is successfully applied as efficient antibacterial agent and selective sensor and adsorbent of rare metal ion, i.e., Dy(III). But the results in this work are generated in batch process using simulated solution containing Dy(III) and other

https://doi.org/10.1021/acsomega.4c02772
ACS Omega 2024, 9, 29620–29632

Table 2. Adsorption Thermodynamics Parameters for Dy(III)-AGO-EPH

concentration (ppm)/ temperature (K)	$-\Delta G^0$ (kJ mol^{-1}) of Dy(III)-AGO-EPH	$-\Delta H^0$ (kJ mol^{-1}) of Dy(III)-AGO-EPH	$-\Delta S^0$ (J mol^{-1} K^{-1}) of Dy(III)-AGO-EPH
5/298	8.61	46.57	127.37
5/303	7.97		
5/308	7.34		
5/313	6.70		
10/298	8.14	36.55	95.34
10/303	7.66		
10/308	7.19		
10/313	6.71		
15/298	7.26	45.39	127.96
15/303	6.62		
15/308	5.98		
15/313	5.34		
20/298	5.82	43.88	127.72
20/303	5.18		
20/308	4.54		
20/313	3.90		
25/298	4.27	32.05	93.22
25/303	3.84		
25/308	3.33		
25/313	2.87		
30/298	3.13	26.27	77.64
30/303	2.75		
30/308	2.36		
30/313	1.97		

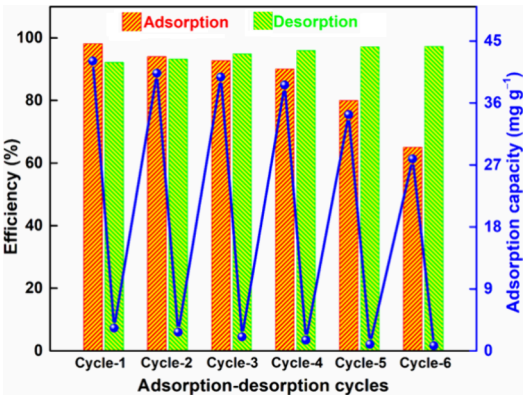

Figure 9. Adsorption−desorption efficiencies (%) of **AGO-EPH** for 6 adsorption−desorption cycles (black *Y*-axis) and (b) Adsorption capacities (mg g^{-1}) of **AGO-EPH** for 6 adsorption−desorption cycles (blue *Y*-axis).

rare earth metal ions, such as Eu(III), Sm(III), Yb(III), Gd(III), Ce(III), Nd(III), and Pr(III). However, its extension to the real industrial effluents containing other elements and the process scale up are yet to be explored.

■ ASSOCIATED CONTENT

Supporting Information

The Supporting Information is available free of charge at https://pubs.acs.org/doi/10.1021/acsomega.4c02772.

Synthetic design for optimization of **EPH** and **AGO-EPH**; Raman and XRD analyses of graphite/GO/AGO; EDX spectrum of graphite, GO, and AGO; FTIR and XRD analyses of **EPH**/**AGO-EPH**/Dy(III)-**AGO-EPH**; MALDI-TOF spectra of **EPH** and **AGO-EPH**; pH_{PZC} analyses of **AGO-EPH**; LOD of Dy(III)-**AGO-EPH**; Antibacterial study of **AGO-EPH** against *E. coli* and cell viability study by MTT assay analyses of **EPH** and **AGO-EPH** (PDF)

■ AUTHOR INFORMATION

Corresponding Author

Chinmay Ghoroi − *DryProTech Lab, Department of Chemical Engineering, Indian Institute of Technology-Gandhinagar, Gandhinagar, Gujarat 382055, India;* orcid.org/0000-0002-2768-5973; Email: chinmayg@iitgn.ac.in

Authors

Mrinmoy Karmakar − *DryProTech Lab, Department of Chemical Engineering, Indian Institute of Technology-Gandhinagar, Gandhinagar, Gujarat 382055, India;* orcid.org/0000-0002-6582-8111

Somya Sadaf − *DryProTech Lab, Department of Chemical Engineering, Indian Institute of Technology-Gandhinagar, Gandhinagar, Gujarat 382055, India;* orcid.org/0009-0003-3589-4358

Complete contact information is available at: https://pubs.acs.org/10.1021/acsomega.4c02772

Notes

The authors declare no competing financial interest.

■ ACKNOWLEDGMENTS

Authors sincerely acknowledge the Common Research & Technological Development Hub (DSIR & IITGN Grant No. DSIR/CRTDH/NM/IIT - GN/2016) and Central Instrumentation Facility in the Indian Institute of Technology, Gandhinagar for technical help in various aspects of this project. The authors would also like to thank the B. S. Gelot

Chair for the valuable support in this work. M.K. is thankful to Indian Institute of Technology Gandhinagar for providing Fellowship for the research. S.S. is grateful to Prime Minister Research fellowship (MIS/IITGN/PMRF/CL/CG/2023-24/048) for financial support.

REFERENCES

(1) Binnemans, K.; Jones, P. T.; Blanpain, B.; Van Gerven, T.; Yang, Y.; Walton, A.; Buchert, M. Recycling of Rare Earths: A Critical Review. *J. Clean. Prod.* **2013**, *51*, 1−22.
(2) Alcaraz, L.; Escudero, M. E.; Alguacil, F. J.; Llorente, I.; Urbieta, A.; Fernández, P.; López, F. A. Dysprosium Removal from Water using Active Carbons Obtained from Spent Coffee Ground. *Nanomaterials* **2019**, *9*, 1372.
(3) Seo, Y.; Morimoto, S. Comparison of Dysprosium Security Strategies in Japan for 2010−2030. *Resour. Policy* **2014**, *39*, 15−20.
(4) Ganesh Kumar, K.; Balaji Bhargav, P.; Aravinth, K.; Arumugam, R.; Ramasamy, P. Dysprosium activated strontium aluminate phosphor: A potential candidate for WLED applications. *J. Lumin.* **2020**, *223*, No. 117126.
(5) Wei, G.; Lapatovich, W.; Browne, J.; Snellgrove, R. Dysprosium oxide ceramic arc tube for HID lamps. *J. Phys. D* **2008**, *41*, No. 144014.
(6) Hoenderdaal, S.; Tercero Espinoza, L.; Marscheider-Weidemann, F.; Graus, W. Can a dysprosium shortage threaten green energy technologies? *Energy* **2013**, *49*, 344−355.
(7) Geysens, P.; Lin, P.-C.; Fransaer, J.; Binnemans, K. Electrodeposition of neodymium and dysprosium from organic electrolytes. *Phys. Chem. Chem. Phys.* **2021**, *23*, 9070−9079.
(8) Briao, G. d. V.; da Silva, M. G.; Vieira, M. G. A. Expanded vermiculite as an alternative adsorbent for the dysprosium recovery. *J. Taiwan Inst. Chem. Eng.* **2021**, *127*, 228−235.
(9) Awual, M. R.; Alharthi, N. H.; Okamoto, Y.; Karim, M. R.; Halim, M. E.; Hasan, M. M.; Rahman, M. M.; Islam, M. M.; Khaleque, M. A.; Sheikh, M. C. Ligand field effect for Dysprosium(III) and Lutetium(III) adsorption and EXAFS coordination with novel composite nanomaterials. *Chem. Eng. J.* **2017**, *320*, 427−435.
(10) Liu, E.; Xu, X.; Zheng, X.; Zhang, F.; Liu, E.; Li, C. An ion imprinted macroporous chitosan membrane for efficiently selective adsorption of dysprosium. *Sep. Purif. Technol.* **2017**, *189*, 288−295.
(11) Dysprosium Market − Forecast (2023−2028). https://www.industryarc.com/Report/16049/dysprosium-market.html .
(12) Malhotra, N.; Hsu, H.-S.; Liang, S.-T.; Roldan, M. J. M.; Lee, J.-S.; Ger, T.-R.; Hsiao, C.-D. An updated review of toxicity effect of the rare earth elements (REEs) on aquatic organisms. *Animals* **2020**, *10*, 1663.
(13) Rim, K. T.; Koo, K. H.; Park, J. S. Toxicological evaluations of rare earths and their health impacts to workers: a literature review. *Saf Health Work* **2013**, *4*, 12−26.
(14) Goonan, T. G. *Rare Earth Elements: End Use and Recyclability*; US Department of the Interior, US Geological Survey: Reston, VA, USA, 2011.
(15) Chen, Y.; Zhang, J.; Zhang, Z.; Chen, J. Studies on monoxide emission spectrometry of rare earth elements Part V. Determination of Dy in rare earth concentrates by dual wavelength method. *Analyst* **1998**, *123*, 1235−1238.
(16) Garcia, E. E.; Nogueira, A. R. A.; Nóbrega, J. A. Matrix effects on the determination of dysprosium, europium and ytterbium used as animal faecal markers by inductively coupled plasma optical emission spectrometry with axially-and radially-viewed configurations. *J. Anal At Spectrom* **2001**, *16*, 825−830.
(17) Purohit, P. J.; Thulasidas, S. K.; Goyal, N.; Page, A. G. Solid sampling approach in inductively coupled plasma atomic emission spectrometry for the determination of four lanthanides with high sensitivity. *J. Anal. At. Spectrom.* **1997**, *12*, 1317−1322.
(18) Zamani, H. A.; Faridbod, F.; Ganjali, M. R. Dysprosium selective potentiometric membrane sensor. *Mater. Sci. Eng., C* **2013**, *33*, 608−612.
(19) Prasad, K.; Kala, R.; Prasada Rao, T.; Naidu, G.R.K. Ion imprinted polymer based ion-selective electrode for the trace determination of dysprosium(III) ions. *Anal. Chim. Acta* **2006**, *566*, 69−74.
(20) Tanner, S. P.; Street, K. W. Solid-phase luminescence of several rare earth ions on ion-exchange films. *J. Appl. Spectrosc.* **2000**, *54*, 669−675.
(21) Ding, Y.; Harvey, D.; Wang, N.-H. L. Two-zone ligand-assisted displacement chromatography for producing high-purity praseodymium, neodymium, and dysprosium with high yield and high productivity from crude mixtures derived from waste magnets. *Green Chem.* **2020**, *22*, 3769−3783.
(22) Sun, S.; Wu, X.; Yang, J.; Li, L.; Wang, Y. Determination of dysprosium by resonance light scattering technique in the presence of BPMPHD. *Spectrochim. Acta A Mol. Biomol. Spectrosc.* **2004**, *60*, 261−264.
(23) Ganjali, M.; Zare-Dorabei, R.; Norouzi, P. Design and construction of a novel optical sensor for determination of trace amounts of dysprosium ion. *Sens. Actuators B Chem.* **2009**, *143*, 233−238.
(24) Knutsen, E.; Wibetoe, G.; Martinsen, I. Determination of elevated levels of dysprosium in serum by electrothermal atomic absorption spectrometry. *J. Anal At Spectrom* **1995**, *10* (10), 757−761.
(25) Vinothkumar, V.; Sakthivel, R.; Chen, S.-M. Rare earth dysprosium nickelate nanospheres for the selective electrochemical detection of antipsychotic drug perphenazine in biological samples. *Mater. Today Chem.* **2022**, *24*, No. 100883.
(26) Mahapatra, M.; Dutta, A.; Mitra, M.; Karmakar, M.; Ghosh, N. N.; Chattopadhyay, P. K.; Singha, N. R. Intrinsically fluorescent biocompatible terpolymers for detection and removal of Bi(III) and cell imaging. *ACS Appl. Bio Mater.* **2020**, *3*, 6155−6166.
(27) Li, J.; Chen, G.; Zeng, Y. e. Simultaneous determination of Dy, Eu, Sm and Tb by laser induced-time resolved derivative fluorescence. *Fresenius J. Anal. Chem.* **1990**, *336*, 139−142.
(28) Karmakar, M.; Mahapatra, M.; Dutta, A.; Chattopadhyay, P. K.; Singha, N. R. Fabrication of semisynthetic collagenic materials for mere/synergistic adsorption: A model approach of determining dye allocation by systematic characterization and optimization. *Int. J. Biol. Macromol.* **2017**, *102*, 438−456.
(29) Qadeer, R.; Hanif, J. Adsorption of dysprosium ions on activated charcoal from aqueous solutions. *Carbon* **1995**, *33*, 215−220.
(30) Kaneko, T.; Hikosaka, R.; Nagata, F.; Inagaki, M.; Kato, K. Effective adsorption of dysprosium ions on amino and carboxyl functionalized mesoporous silica sheets. *J. Asian Ceram. Soc.* **2019**, *7*, 213−220.
(31) Singha, N. R.; Karmakar, M.; Mahapatra, M.; Mondal, H.; Dutta, A.; Deb, M.; Mitra, M.; Roy, C.; Chattopadhyay, P. K. An in-situ approach for the synthesis of a gum ghatti-g-interpenetrating terpolymer network hydrogel for the high-performance adsorption mechanism evaluation of Cd (II), Pb (II), Bi (III) and Sb (III). *J. Mater. Chem. A* **2018**, *6*, 8078−8100.
(32) Mondal, H.; Karmakar, M.; Chattopadhyay, P. K.; Halder, A.; Singha, N. R. Scale-up one-pot synthesis of waste collagen and apple pomace pectin incorporated pentapolymer biocomposites: Roles of waste collagen for elevations of properties and unary/ternary removals of Ti(IV), As(V), and V(V). *J. Hazard. Mater.* **2021**, *409*, No. 124873.
(33) Karmakar, M.; Mondal, H.; Mahapatra, M.; Chattopadhyay, P. K.; Chatterjee, S.; Singha, N. R. Pectin-grafted terpolymer superadsorbent via N−H activated strategic protrusion of monomer for removals of Cd(II), Hg(II), and Pb(II). *Carbohydr. Polym.* **2019**, *206*, 778−791.
(34) Tang, W.; Gu, Z.; Chu, Y.; Lv, J.; Fan, L.; liu, X.; Wang, F.; Ying, Y.; Zhang, J.; Jiang, Y.; Cao, J.; Zhu, A.; Yang, H. Magnetically-oriented porous hydrogel advances wearable electrochemical solidoid sensing heavy metallic ions. *Chem. Eng. J.* **2023**, *453*, No. 139902.
(35) Qi, S.; Zhang, Y.; Shi, J.; Wang, Y.; Gao, J.; Fan, W.; Sui, K.; Qi, P. Autonomous enrichment and deep removal of heavy metals by salt-

https://doi.org/10.1021/acsomega.4c02772
ACS Omega 2024, 9, 29620−29632

tolerant gradient polyelectrolyte hydrogels. *J. Chem. Eng.* **2023**, *472*, No. 145158.
(36) Mondal, H.; Karmakar, M.; Chattopadhyay, P. K.; Singha, N. R. Starch-g-tetrapolymer hydrogel via in situ attached monomers for removals of Bi (III) and/or Hg (II) and dye (s): RSM-based optimization. *Carbohydr. Polym.* **2019**, *213*, 428−440.
(37) Mondal, H.; Karmakar, M.; Chattopadhyay, P. K.; Singha, N. R. Synthesis of pH-responsive sodium alginate-g-tetrapolymers via NC and OC coupled in situ monomers: A reusable optimum hydrogel for removal of plant stressors. *J. Mol. Liq.* **2020**, *319*, No. 114097.
(38) Mondal, H.; Karmakar, M.; Chattopadhyay, P. K.; Singha, N. R. New property-performance optimization of scalable alginate-g-terpolymer for Ce(IV), Mo(VI), and W(VI) exclusions. *Carbohydr. Polym.* **2020**, *245*, No. 116370.
(39) Sturala, J.; Luxa, J.; Pumera, M.; Sofer, Z. Chemistry of graphene derivatives: Synthesis, applications, and perspectives. *Chem.-Eur. J.* **2018**, *24*, 5992−6006.
(40) Xu, Y.; Shi, G. Assembly of chemically modified graphene: methods and applications. *J. Mater. Chem.* **2011**, *21*, 3311−3323.
(41) Hadadian, M.; Goharshadi, E. K.; Youssefi, A. Electrical conductivity, thermal conductivity, and rheological properties of graphene oxide-based nanofluids. *J. Nanopart. Res.* **2014**, *16*, 1−17.
(42) Zaaba, N.; Foo, K.; Hashim, U.; Tan, S.; Liu, W.-W.; Voon, C. Synthesis of graphene oxide using modified hummers method: solvent influence. *Procedia Eng.* **2017**, *184*, 469−477.
(43) Zhang, C.; Hao, R.; Liao, H.; Hou, Y. Synthesis of amino-functionalized graphene as metal-free catalyst and exploration of the roles of various nitrogen states in oxygen reduction reaction. *Nano Energy* **2013**, *2*, 88−97.
(44) Singha, N. R.; Karmakar, M.; Mahapatra, M.; Mondal, H.; Dutta, A.; Roy, C.; Chattopadhyay, P. K. Systematic synthesis of pectin-g-(sodium acrylate-co-N-isopropylacrylamide) interpenetrating polymer network for superadsorption of dyes/M(II): determination of physicochemical changes in loaded hydrogels. *Polym. Chem.* **2017**, *8*, 3211−3237.
(45) Karmakar, M.; Mondal, H.; Ghosh, T.; Chattopadhyay, P. K.; Maiti, D. K.; Singha, N. R. Chitosan-grafted tetrapolymer using two monomers: pH-responsive high-performance removals of Cu(II), Cd(II), Pb(II), dichromate, and biphosphate and analyses of adsorbed microstructures. *Environ. Res.* **2019**, *179*, No. 108839.
(46) Akhavan, O. Bacteriorhodopsin as a superior substitute for hydrazine in chemical reduction of single-layer graphene oxide sheets. *Carbon* **2015**, *81*, 158−166.
(47) Muzyka, R.; Drewniak, S.; Pustelny, T.; Chrubasik, M.; Gryglewicz, G. Characterization of graphite oxide and reduced graphene oxide obtained from different graphite precursors and oxidized by different methods using Raman spectroscopy. *Materials* **2018**, *11*, 1050.
(48) Pravin, M. D.; Gnanamani, A.; Felshia, C. S. Preparation, characterization and reusability efficacy of amine-functionalized graphene oxide-polyphenol oxidase complex for removal of phenol from aqueous phase. *RSC Adv.* **2018**, *8*, 38416−38424.
(49) Rani, S.; Kumar, M.; Garg, R.; Sharma, S.; Kumar, D. Amide functionalized graphene oxide thin films for hydrogen sulfide gas sensing applications. *IEEE Sens. J.* **2016**, *16*, 2929−2934.
(50) Aliyev, E. M.; Khan, M. M.; Nabiyev, A. M.; Alosmanov, R. M.; Bunyad-zadeh, I. A.; Shishatskiy, S.; Filiz, V. Covalently Modified Graphene Oxide and Polymer of Intrinsic Microporosity (PIM-1) in Mixed Matrix Thin-Film Composite Membranes. *Nanoscale Res. Lett.* **2018**, *13*, 359.
(51) Huang, H.; Wang, Y.; Zhang, Y.; Niu, Z.; Li, X. Amino-functionalized graphene oxide for Cr(VI), Cu(II), Pb(II) and Cd(II) removal from industrial wastewater. *Open Chem.* **2020**, *18*, 97−107.
(52) Singha, N. R.; Mahapatra, M.; Karmakar, M.; Dutta, A.; Mondal, H.; Chattopadhyay, P. K. Synthesis of guar gum-g-(acrylic acid-co-acrylamide-co-3-acrylamido propanoic acid) IPN via in situ attachment of acrylamido propanoic acid for analyzing super-adsorption mechanism of Pb (II)/Cd(II)/Cu(II)/MB/MV. *Polym. Chem.* **2017**, *8*, 6750−6777.
(53) Mondal, H.; Karmakar, M.; Dutta, A.; Mahapatra, M.; Deb, M.; Mitra, M.; Roy, J. S. D.; Roy, C.; Chattopadhyay, P. K.; Singha, N. R. Tetrapolymer network hydrogels via gum ghatti-grafted and N−H/C−H-activated allocation of monomers for composition-dependent superadsorption of metal ions. *ACS omega* **2018**, *3*, 10692−10708.
(54) Swift, T.; Swanson, L.; Geoghegan, M.; Rimmer, S. The pH-responsive behaviour of poly(acrylic acid) in aqueous solution is dependent on molar mass. *Soft Matter* **2016**, *12*, 2542−2549.
(55) Tran, B.; Cai, Y.; Janik, M. J.; Milner, S. T. Hydrogen Bond Thermodynamics in Aqueous Acid Solutions: A Combined DFT and Classical Force-Field Approach. *J. Phys. Chem. A* **2022**, *126*, 7382−7398.
(56) Zhang, L.; Wei, L.-G.; Zhai, S.-R.; Zhao, D.-W.; Sun, J.; An, Q.-D. Hydrogen bond promoted thermal stability enhancement of acetate based ionic liquid. *Chin. J. Chem. Eng.* **2020**, *28*, 1293−1301.
(57) Salavati-Niasari, M.; Javidi, J. Synthesis of hollow SiO_2 nanoparticles from Dy_2O_3@SiO_2 core−shell nanocomposites via a recyclable sonochemical method. *J. Clust. Sci.* **2012**, *23*, 1019−1028.
(58) Karmakar, M.; Mondal, H.; Ghosh, N. N.; Chattopadhyay, P. K.; Singha, N. R. Synthesis of gum tragacanth-grafted pentapolymer hydrogels for As (III) exclusion: Roles of microwaves, RSM optimization, and DFT studies. *Int. J. Biol. Macromol.* **2021**, *184*, 909−925.
(59) Mondal, H.; Karmakar, M.; Ghosh, N. N.; Maiti, D. K.; Chattopadhyay, P. K.; Singha, N. R. One-pot synthesis of sodium alginate-grafted-terpolymer hydrogel for As(III) and V(V) removal: In situ anchored comonomer and DFT studies on structures. *J. Environ. Manage.* **2021**, *294*, No. 112932.
(60) Mondal, H.; Datta, B. Banana Peel Derived Chitosan-Grafted Biocomposite for Recovery of NH_4^+ and PO_4^{3-}. *ACS Omega* **2023**, *8*, 43674−43689.
(61) Mondal, H.; Karmakar, M.; Datta, B. An MXene-Grafted Terpolymer Hydrogel for Adsorptive Immobilization of Toxic Pb(II) and Post-Adsorption Application of Metal Ion Hydrogel. *Gels* **2023**, *9*, 827.

https://doi.org/10.1021/acsomega.4c02772
ACS Omega 2024, 9, 29620−29632